ACS APPLIED MATERIALS & INTERFACES

www.acsami.org Research Article

# Colorimetric Detection of SARS-CoV-2 Using Plasmonic Biosensors and Smartphones

Elsa M. Materón,* Faustino R. Gómez, Mariana B. Almeida, Flavio M. Shimizu, Ademar Wong, Kelcilene B. R. Teodoro, Filipe S. R. Silva, Manoel J. A. Lima, Monara Kaelle S. C. Angelim, Matias E. Melendez, Nelson Porras, Pedro M. Vieira, Daniel S. Correa, Emanuel Carrilho, Osvaldo N. Oliveira, Jr., Ricardo B. Azevedo, and Débora Goncalves

Cite This: https://doi.org/10.1021/acsami.2c15407 Read Online

ACCESS | Metrics & More | Article Recommendations | Supporting Information

**ABSTRACT:** Low-cost, instrument-free colorimetric tests were developed to detect SARS-CoV-2 using plasmonic biosensors with Au nanoparticles functionalized with polyclonal antibodies (f-AuNPs). Intense color changes were noted with the naked eye owing to plasmon coupling when f-AuNPs form clusters on the virus, with high sensitivity and a detection limit of 0.28 PFU $mL^{-1}$ (PFU stands for plaque-forming units) in human saliva. Plasmon coupling was corroborated with computer simulations using the finite-difference time-domain (FDTD) method. The strategies based on preparing plasmonic biosensors with f-AuNPs are robust to permit SARS-CoV-2 detection via dynamic light scattering and UV−vis spectroscopy without interference from other viruses, such as influenza and dengue viruses. The diagnosis was made with a smartphone app after processing the images collected from the smartphone camera, measuring the concentration of SARS-CoV-2. Both image processing and machine learning algorithms were found to provide COVID-19 diagnosis with 100% accuracy for saliva samples. In subsidiary experiments, we observed that the biosensor could be used to detect the virus in river waters without pretreatment. With fast responses and requiring small sample amounts (only 20 $\mu$L), these colorimetric tests can be deployed in any location within the point-of-care diagnosis paradigm for epidemiological control.

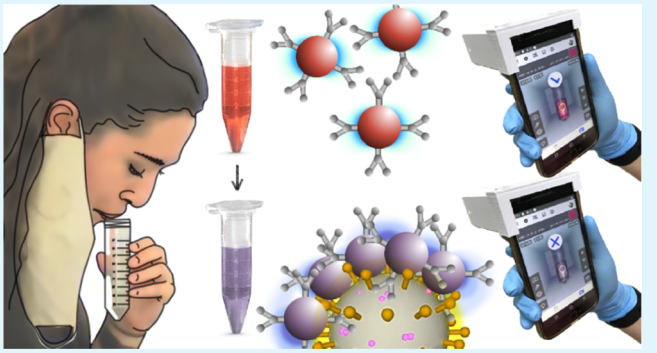

**KEYWORDS:** *gold nanoparticles, localized surface plasmon resonance, plasmonic coupling, SARS-CoV-2, point-of-care, machine learning, image processing, portable sensor*

## 1. INTRODUCTION

Mass testing for viral diseases remains relevant given the persistence of contamination with the severe acute respiratory syndrome coronavirus 2 (SARS-CoV-2 virus). Most diagnostic tests require cheaper detection methods than prevailing molecular techniques, such as reverse transcription-quantitative polymerase chain reaction (RT-qPCR), isothermal amplification-based methods, and CRISPR-based diagnostics.[1] Antigen-based detection (antigen test) has become commonplace in lateral flow immunoassays (LFI) or immunostrips,[2] but it achieves less sensitive responses than the reverse-transcription polymerase chain reaction (RT-PCR).[3] Current tests employ mostly blood and nasopharyngeal samples, which are uncomfortable for many patients. Less invasive sample collection is preferable, as saliva sampling is accessible to self-collect, particularly in fragile and vulnerable patient populations.[4] The pathogen levels in saliva are comparable to those in nasopharyngeal samples, with the advantage of a small variability across trials.[5] In addition, the costs of collection and storage are also reduced.

Challenges are often found in processing and avoiding degradation in saliva, which has hampered diagnostic tools.[6] Furthermore, effective detection of SARS-CoV-2 in saliva requires high sensitivity because of its enzymes that may destabilize nucleic acid and inhibit proteases.[7,8] For SARS-CoV-2, most infectious saliva and cough specimens have virus loads near $10^6$ PFU $mL^{-1}$ (PFU stands for plaque-forming units), indicating that 10−100 $\mu$L droplets could deposit $10^4$−$10^5$ PFU of infectious material.[9−11] The minimal contagious dose in humans ranges from 1 to 5 PFU.[12]

Received: August 26, 2022
Accepted: November 8, 2022

Although SARS-CoV-2 infection occurs predominantly through the respiratory tract, the entry of virus into the bloodstream compromises other organs, and viral RNA has been detected in the feces of infected individuals, even after respiratory symptoms have diminished.[13] Likewise, SARS-CoV-2 has been detected for prolonged periods in wastewater treatment plants[14] and river waters.[15] Excretions through feces occur due to the viral infection into the gastrointestinal tract via the angiotensin-converting enzyme 2 (ACE2) receptor expressed by epithelial cells in the gastrointestinal system,[16] and even *via* urine and saliva. Hence, virus particles can be dragged to treatment plants and may not be cleared during water treatment.[16] Therefore, detecting SARS-CoV-2 is not only relevant for diagnosis in humans but also for verifying possible contamination of water resources.

Pathogens and other biomarkers can be detected with several principles, including electrical,[17] electrochemical,[18] optical,[19] and thermoplasmonic chips.[20] Colorimetric tests are preferred in many scenarios owing to the simplicity of the analysis.[21] Nevertheless, it is challenging if the detection processes must yield significant color changes. For colorimetric tests, the use of nanoparticles is noteworthy,[22] including Ag nanoparticles,[23] Au nanoparticles (AuNPs),[24] quantum dots,[25] magnetic nanoparticles,[26] and Au nanorods,[27] which have been used to detect SARS-CoV-2 virus or IgG antibodies with localized surface plasmon resonance (LSPR) and surface-enhanced Raman spectroscopy (SERS). AuNPs are known for their chemical stability, easy modification, and bioconjugation of biomolecules, such as DNA, antibody, enzymes, and other proteins.[28] For example, immunogenic B cell epitopes can be attached to AuNPs to detect COVID-19-specific IgG where the optical properties of AuNPs are exploited.[29] Also, colloidal Au can be prepared with controllable sizes using the well-known citrate reduction method.[30] AuNPs show a high-surface density of free electrons, from which LSPR has emerged.[31] LSPR is produced by the collective oscillation of surface electrons induced by visible light, manifested by an extinction band in the visible region. It is relevant that LSPR depends on the refractive index of the surrounding medium and the interparticle distance, providing the basis for colorimetric plasmonic sensors.[32−34] In such colorimetric sensors, observation with the naked eye can be done with changes in the liquid phase within 5 min, *i.e.*, one may distinguish between positive and negative results.[35] AuNPs have been employed in detecting viruses such as Zika (ZIKV), Ebola (EBOV), Influenza A virus (H1N1), and severe acute respiratory syndrome coronavirus 2 (SARS-CoV-2).[31] Antibodies coupled to AuNPs can bind to the viral antigen leading to agglomeration of NPs, thus shifting its color from red to blue.[24]

Herein, low-cost, instrument-free, fast-response plasmonic biosensors were designed to detect SARS-CoV-2 in saliva and river water without sample pretreatment. Detection was primarily based on naked-eye colorimetry. Meanwhile, more detailed considerations of the detection processes were studied using UV−vis spectroscopy. For naked-eye colorimetry, we used a free smartphone application to process the images acquired with the smartphone camera, thus allowing instant results similar to other examples described in the literature (see Table S1 in the Supporting Information). The mechanisms responsible for the colloidal nanoparticle clustering around the virus, then allowing their detection with high sensitivity, are investigated for the first time using theoretical simulations with the finite-difference time-domain (FDTD) method. The most relevant contribution of this work is associated with the fast detection of SARS-CoV-2 without requiring instruments, with the high accuracy warranted by treating images with machine learning algorithms.

## 2. MATERIALS AND METHODS

Gold(III) chloride trihydrate ($HAuCl_4 \cdot 3H_2O$, ≥99.9% purity), 11-mercaptoundecanoic acid (MUA, ≥95%), sodium citrate dihydrate (≥99%), *N*-(3-dimethylaminopropyl)-*N*′-ethylcarbodiimide hydrochloride (EDC, ≥98%), *N*-hydroxysuccinimide (NHS, 98%), bovine serum albumin (BSA, ≥98%), poly(ethylene glycol) methyl ether thiol, average Mn 6000 (PEG-SH), and phosphate-buffered saline powder (pH 7.4) (P3813−10PAK) were purchased from Sigma-Aldrich. Recombinant anti-SARS-CoV-2 Spike glycoprotein S1 antibody (ab273073), recombinant human coronavirus SARS-CoV-2 Spike glycoproteins S1 (Active) (ab273068), and RBD (Active) (ab273065) were acquired from Abcam. Polyclonal antibody against the N-terminal domain of the SARS-CoV-2 Spike protein from rabbits was kindly provided by Virology and Microscopy Laboratory, Universidade de Brasília, Brazil. H1N1 California (OPPA01974) and Dengue envelope-3 (DENV, OPPA02454) proteins were acquired from Aviva Systems Biology. Gold seed particles were prepared using a modified Turkevich synthesis[36] by adding gold chloride via sodium citrate reduction. The growth of Au nanoparticles (AuNPs) occurred after mixing two solutions, *viz.* $2.2 \times 10^{-3}$ mol $L^{-1}$ citrate and $25 \times 10^{-3}$ mol $L^{-1}$ $HAuCl_4$, seven times with a 30-min break.[1] The solution containing AuNPs was cooled by adding 50 mL of ultrapure water. The solution was kept at 4 °C in the dark for further work.

**2.1. Transmission Electron Microscopy (TEM) and Field-Emission Scanning Electron Microscopy (SEM-FEG).** TEM images of AuNPs were collected using a Philips CM200 Transmission Electron microscope designed to obtain high-resolution images with a Super Twin polar piece using an electron beam energy of 25 keV. TEM sample grids were prepared by depositing 10 mL of AuNP suspension onto carbon-coated copper grids, followed by air-drying at room temperature. The average diameter was determined using ImageJ software. SEM-FEG images were obtained using a JEOL JSM-7500F microscope with operating software PC-SEM equipped with secondary and back-scattered electron detectors. Chemical analysis by energy-dispersive spectroscopy (EDS) was performed using an UltraDry detector from Thermo Scientific with NSS 2.3 operating software. Colloidal AuNPs were washed twice, diluted in ultrapure water, and deposited onto glassy carbon supports for later drying at room temperature.

**2.2. UV/Vis Spectroscopy (UV/VIS) and Dynamic Light Scattering (DLS) Measurements.** The UV−vis spectra were collected using a spectrophotometer (Thermo Scientific, Nanodrop 2000/2000c) from 200−800 nm using a 1-cm quartz cuvette. The nanoparticles were washed twice in $5 \times 10^{-3}$ mol $L^{-1}$ phosphate-buffered saline (PBS) at pH 7.4, and 20 $\mu$L of AuNP solutions were diluted in 980 $\mu$L of $5 \times 10^{-3}$ mol $L^{-1}$ PBS at pH 7.4. All AuNP suspensions were analyzed by dynamic light scattering (DLS) using a Nano ZS Malvern Zetasizer using the same washing procedure described before for the UV−vis measurements.

**2.3. Attenuated Total Reflectance (ATR).** The attenuated total reflectance spectra were recorded from 4300 to 600 $cm^{-1}$ using a Bruker Vertex 70 FTIR spectrometer equipped with an attenuated total reflectance (ATR) accessory. The measurements were performed using a blank citrate/AuNP solution. For each measurement, the AuNPs were washed twice in ultrapure water to remove excess PBS and reduce its signals. The samples were prepared by depositing 20 $\mu$L of the AuNP suspension onto the crystal, and measurements were acquired for the colloidal samples at a resolution of 4 $cm^{-1}$ with 64 co-added scans/spectrum.

**2.4. Inactivation of SARS-CoV-2 Virus and Sample Preparation.** The inactivated virus samples used in our studies were obtained from HIAE-02 SARS-CoV-2/SP02/human/2020/BRA (GenBank:


https://doi.org/10.1021/acsami.2c15407
ACS Appl. Mater. Interfaces XXXX, XXX, XXX−XXX

616 MT126808.1) isolated from the second confirmed case in Brazil. The viral stocks of SARS-CoV-2 were propagated in Vero cell lines, and the supernatant was harvested at 2−3 days post-infection. Viral titers were determined by plaque assays on Vero cells, in which the number of plaque-forming units (PFU) represents the viral quantity. Vero CCL-81 cells were cultivated in Dulbecco's modified Eagle's medium (DMEM) (10% fetal bovine serum (FBS), 1% penicillin−streptomycin) and incubated at 37 °C with a 5% $CO_2$ atmosphere. As a control, a conditioned medium of Vero cells was used after being treated in the same way but without the virus. Virus inactivation was performed using a CL1000 UVP crosslinker under UV irradiation in a microbiological safety cabinet, following Patterson et al.[37] The virus stock was added (1500 μL) on 100 mm culture dishes and placed without its lid 6 cm below the UV bulbs. With this procedure, the viruses are inactivated by UV irradiation, and their protein structure is preserved.[38,39] Inactivated SARS-CoV-2 was obtained from the Institute of Biology, University of Campinas (Brazil). Subsequently, a stock solution of the virus was prepared with 10 μL diluted in 990 μL 5.0 × $10^{-3}$ mol $L^{-1}$ PBS at pH 7.4, 7000 PFU.

**2.5. Modification of Colloidal Au Nanoparticles.** Twenty-four microtubes with 1 mL of AuNPs each were used with the following procedure: 1.0 mL of nanoparticles was added to 56.7 μL of 1.9 × $10^{-3}$ mol $L^{-1}$ MUA (dissolved in ethanol) under stirring at 28 °C for 2 h. Then, 55 μL of 2.0 × $10^{-4}$ mol $L^{-1}$ PEG-SH was added to the solution of AuNPs/MUA (dissolved in ultrapure water) for another 2 h under stirring at 28 °C.[40] Volumes of 19 μL of 2.5 × $10^{-3}$ mol $L^{-1}$ EDC and 35 μL of 1.0 × $10^{-2}$ mol $L^{-1}$ NHS in ultrapure water were added to the AuNPs/MUA/PEG-SH solution, which was stirred at 28 °C for 20 min. The mixture was then centrifuged at 7.300 rpm for 20 min at 15 °C. The AuNPs were resuspended in 5 × $10^{-3}$ mol $L^{-1}$ PBS at pH 7.4 with SARS-CoV-2 spike polyclonal antibody (ab) added to obtain a final concentration of 2 μg $mL^{-1}$ (AuNPs/MUA/PEG-ab), followed by incubation overnight at 28 °C. The AuNPs/MUA/PEG-ab solution was centrifuged for 20 min at 7300 rpm at 15 °C. The supernatant was discarded, and the sediment was resuspended in 200 μL of PBS and 300 μL of 0.5% BSA at a final percentage of 0.2%. The f-AuNP (AuNPs/MUA/PEG/ab/BSA) solution was centrifuged, resuspended twice to remove antibodies in excess, and stored at 4 °C.

**2.6. Detection of SARS-CoV-2 in Saliva and Spiked River Samples.** *2.6.1. Synthetic and Human Saliva.* Synthetic saliva was prepared with 0.228 g of $CaCl_2{\cdot}2H_2O$, 0.061 g of $MgCl_2{\cdot}6H_2O$, 1.017 g of NaCl, 0.504 g of $K_2CO_3$, 0.272 g of $Na_2HPO_4{\cdot}12H_2O$, and 0.273 g of $NaH_2PO_4{\cdot}H_2O$.[41] All reagents were diluted in 1 L and used only for comparison with human saliva with a negative Covid test.[41] Then, a volume of 20 μL of artificial saliva was diluted in 960 μL of 5.0 × $10^{-3}$ mol $L^{-1}$ PBS and 20 μL of the f-AuNP solution was added. This solution was compared with the human saliva of healthy donors without symptoms and negative tests, obtaining comparable results. In samples with saliva from a donor tested negative, different concentrations of the inactivated virus were spiked to the samples. In the proof-of-concept experiments, a similar procedure was performed using eleven samples of human saliva: five from individuals without symptoms ($S_1$−$S_5$), three from volunteers with no symptoms and negative PCR tests ($S_p$, $S_m$, and $S_B$), and three from volunteers with positive Covid tests ($C_1$, $C_2$, and $C_3$). The saliva donors followed the protocols required by pharmacies for tests, *viz.*, they should not eat, drink coffee, or brush their teeth for 2 h prior to saliva collection. Also, they should not use lipstick, gloss, or menthol products.[5] Samples were collected in 2 mL tubes and measured immediately.[42]

*2.6.2. River Samples.* River water samples were collected from the Gregorio River (GPS coordinate: 21°59′11.0″ S 47°52′52.1″ W) located in the city of São Carlos-SP (Brazil). A volume of 50 μL of a river sample was diluted in 930 μL of 5.0 × $10^{-3}$ mol $L^{-1}$ PBS to which 20 μL of the f-AuNP solution was added.[43] Then, different concentrations of the inactivated virus were spiked into the river water samples.

**2.7. Quantification of Proteins on AuNPs.** The AuNP−antibody solutions were centrifuged at 7300 rpm for 20 min, the supernatant was removed, and the remaining pellet was resuspended with 5 × $10^{-3}$ mol $L^{-1}$ PBS. This procedure was repeated three times to remove unreacted EDS and NHS, with only AuNP−antibody complexes left. The washed solution was diluted at 1:5 and 1:10 vol/vol, and the antibody concentration was calculated using the bicinchoninic acid (BCA) protein assay according to the manufacturer's protocol (Pierce). The absorbance was measured for diluted solutions at 562 nm using a NanoDrop 2000c Spectrophotometer in the cuvette mode, and the concentration of the bound antibody was calculated by multiplying the concentration by the dilution factor. Mean and standard deviations for the concentration were calculated considering both samples. The BCA assay showed an average antibody concentration of 9.3 ± 0.4 μg $mL^{-1}$ ($n$ = 2) on the surface of AuNPs. This value should be considered with care once the number of antibodies may be overestimated in the BCA protein assay and enzyme-linked immunosorbent assay (ELISA);[44] it serves to confirm modification for nanoparticles coated with antibodies.[45]

**2.8. Smartphone-Based Detection and Statistical Analysis.** Smartphone-based sensing was conducted by getting images directly from the microcentrifuge tube using a Samsung smartphone (Galaxy J8, 16 megapixels camera, with Android 10). The RGB (red, green, blue) mean values were taken as an analytical signal in real-time through the free application (App) Color Grab (Loomatix, version 3.9.2), available for Android systems. For acquiring the digital images in microtubes, we used a built-in polylactic acid (PLA) support fabricated with a three-dimensional (3D) printer (Creality Ender-3) with the following dimensions: height of 5 cm and a 10-cm distance between the smartphone camera and the microtube (see Figure S1 in the Supporting Information). A printable copy of the file (.stl) is available in the Supporting Information (Figure S1). The images were analyzed with the software ImageJ using a 50-pixel circular region, and the RGB (red, green, blue) values were used as the analytical response ($X$). The best linear relationship to $X$ is shown in eq 1, where the letters $B$ and $R$ denote the blue channel and red channel, respectively, and the subscripts "s" and "b" correspond to the values of the sample or standard and the analytical blank, respectively. The blue channel ($B_s$) and red channel ($R_s$) are the values of the sample, while the blank of the blue channel is $B_b$ and the blank of the red channel is $R_b$ (See Figure S1).

$$X = \frac{B_s}{R_s} - \frac{B_b}{R_b} \quad (1)$$

The limit of detection (LOD) of the assay was calculated based on the standard deviation of the blank or the control sample ($SD_b$) and the angular coefficient ($b$—slope) obtained from the analytical curve (ICH 2005),[46] according to eq 2.

$$\mathrm{LOD} = \frac{3.3 \times \mathrm{SD_b}}{b} \quad (2)$$

The experiments were conducted in triplicate, and the relevant data were expressed as the mean ± SD. The statistical analyses were performed using Origin 9.0 and Statistica 13.5.0.17 (TIBCO) software.

**2.9. FDTD Simulations.** The absorption spectra and electromagnetic field distribution for isolated AuNPs and aggregates were calculated using a software package, FDTD Solutions by Ansys Lumerical Solutions. The simulation region was a 2 μm cube surrounded by a perfectly matched layer (PML) filled with water (refractive index RI = 1.33). The mesh size was set to 0.5 nm in all spatial dimensions. The AuNPs were simulated as homogenous spheres of 31 nm diameter, and the dielectric function of Au was adopted from the experimental data obtained by Johnson and Christy.[47] The molecular linkers and antibodies anchored to the Au surface were simulated as a dielectric shell with a refractive index of 1.4 and 1.5 nm thick. The virus was simulated as a homogeneous dielectric sphere with a 100-nm diameter and a refractive index of 1.54, surrounded by a 10-nm thick dielectric shell with a refractive index of 1.46.[48] Functionalized AuNP (f-AuNP) clusters were randomly placed on the virus surface to simulate the aggregate system. The algorithm for generating the clusters first added a functionalized NP onto the virus surface from a randomized position.


https://doi.org/10.1021/acsami.2c15407
ACS Appl. Mater. Interfaces XXXX, XXX, XXX−XXX

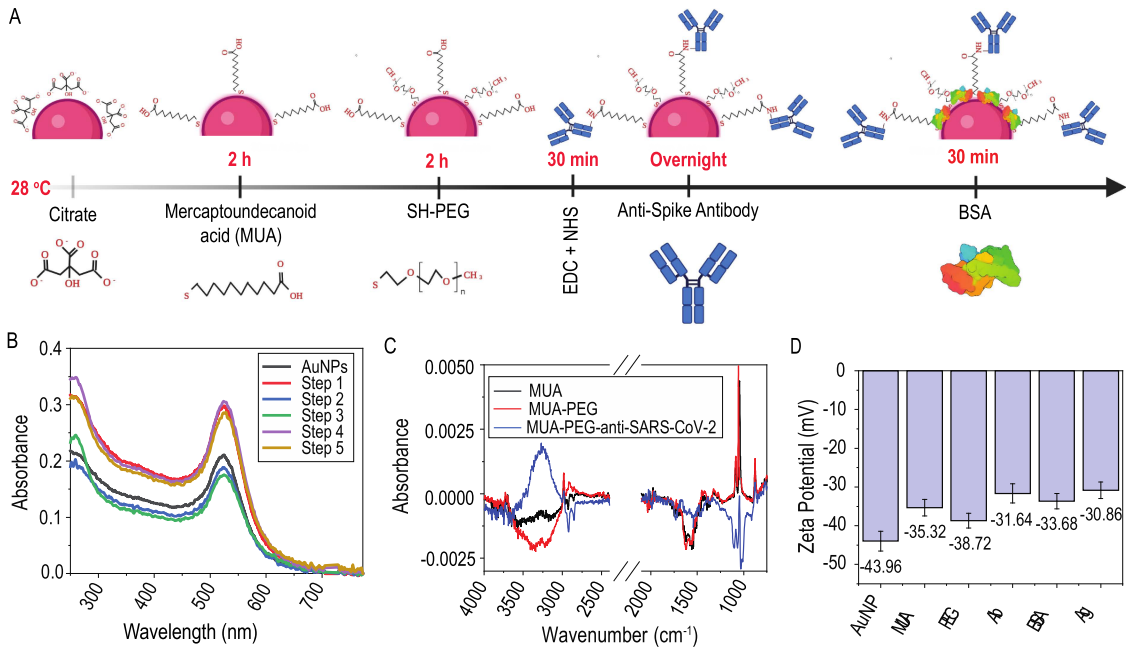


**Figure 1.** (A) Schematic design for modification of AuNPs, throughout the various steps. (B) UV−vis spectra for the distinct steps in the bioconjugation (AuNPs after addition of: step 1 MUA, step 2 PEG-SH, step 3 EDC/NHS, step 4 antibody, and step 5 BSA). (C) ATR spectra for AuNPs coated with MUA, then MUA−PEG and MUA−PEG-anti-SARS-CoV-2. (D) $\zeta$-potential at each step of AuNP bioconjugation and in the presence of 3.2 $\mu$g mL$^{-1}$ S protein of SARS-CoV-2 virus.

Subsequently, a second NP was located randomly around the initial particle. The cluster was grown until a specified number of NPs was reached. The cluster formation randomly achieved the interparticle distance between 1 and 2 nm. A total-field scattered field (TFSF) source with a wavelength ranging from 350 to 850 nm was used to illuminate the systems. The incident plane wave was *x*-polarized, and the propagation direction was set along the minus *z*-axis. The electric field strength of the incident irradiation was set at 1.0 V m$^{-1}$. A 3D frequency-domain field profile monitor and a group analysis (both inside the TSFS source) were used to record the electric field and calculate the absorption cross-section, respectively. All of the absorption cross-section spectra are reported as a dimensionless Mie efficiency calculated by dividing the optical cross-section by $N\pi R^2$, where $R$ is the radius of the NPs and $N$ is the number of NPs in a cluster.[49]

## 3. RESULTS AND DISCUSSION

**3.1. Bioconjugation and Images of AuNPs.** The FEG-SEM and TEM images show spherical AuNPs with an average diameter of 31 nm (Figure S2A,B in the Supporting Information). The high purity of AuNPs was confirmed with a strong signal of elemental Au in Figure S2C (EDS analysis), with stability in the pH range between 3.0 and 8.0 in 5.0 × 10$^{-3}$ mol L$^{-1}$ PBS, as indicated in Figure S2D. The AuNPs were functionalized by covalent coupling of antibodies using a mercaptoundecanoic acid binder (MUA), following the procedure depicted in Figure 1A. The whole procedure was monitored using UV−vis spectroscopy and $\zeta$-potential measurements. MUA was bound covalently onto AuNPs through its thiol groups to the Au surface; its quaternary ammonium counterion adsorbed on the Stern layer provided stability against aggregation.[50] AuNPs coated with MUA had a 35-nm diameter, which confirmed an increase in shell thickness. MUA coating is not expected to be homogeneous but on patches according to dissipative particle dynamics simulations.[51] Figure 1B shows the plasmonic peak of monodisperse AuNPs at 524 nm shifted to 526 nm for AuNPs−MUA,[52] with the increased absorbance after MUA modification occurring due to aggregation of AuNPs. PEG-SH occupies the remaining free AuNP surface, exhibiting a radial conformation since the thiol group has a stronger affinity for the AuNP surface than PEG chains, thus removing these from the NP surface.[51] A decrease in absorbance was observed upon adding PEG[53] due to aggregation of polydisperse PEG−AuNPs[54] and after activating terminal carboxylic acid head-groups by EDC/NHS at pH ∼ 6.0. The p$K_a$ of EDC is 6.0, and that of MUA on Au is 4.5−6.0. Hence, deprotonation of 11-MUA and protonation of EDC seem to be important in the activation reaction.[55] The formation of nanoensembles can cause a decrease in absorbance due to their activating ability.[56] EDC/NHS binding has the advantage of providing a stable, biocompatible, covalent bond.[57] The activation mechanism of carboxyl groups mediated by EDC/NHS involves the formation of an adduct, an *O*-acylisourea derivative, between EDC and the carboxyl group of MUA.[58] The *O*-acylurea adduct reacts with a primary amine and produces the desired peptide coupling, but it has a low reaction rate. Hence, NHS provides a more stable intermediate to react with a primary amine forming an amide bond.[59] Then, a nucleophilic attack by NHS may occur to form an *N*-succinimidyl ester, releasing a soluble urea derivative as a by-product.[58]

The incorporation of antibodies increased the absorbance intensity significantly due to an increased effect on the hydrodynamic-layer thickness of the AuNPs and changed their refractive index after conjugation.[60] In subsidiary experiments, we observed that efficient plasmonic biosensors can be obtained with either monoclonal or rabbit polyclonal antibodies. The results in detecting inactivated viruses via DLS are shown in Figure S3. We have therefore employed the polyclonal antibody in the subsequent studies. The remaining active sites after the antibody adsorption were blocked by BSA addition, which caused a decrease in absorbance. The


https://doi.org/10.1021/acsami.2c15407
ACS Appl. Mater. Interfaces XXXX, XXX, XXX−XXX

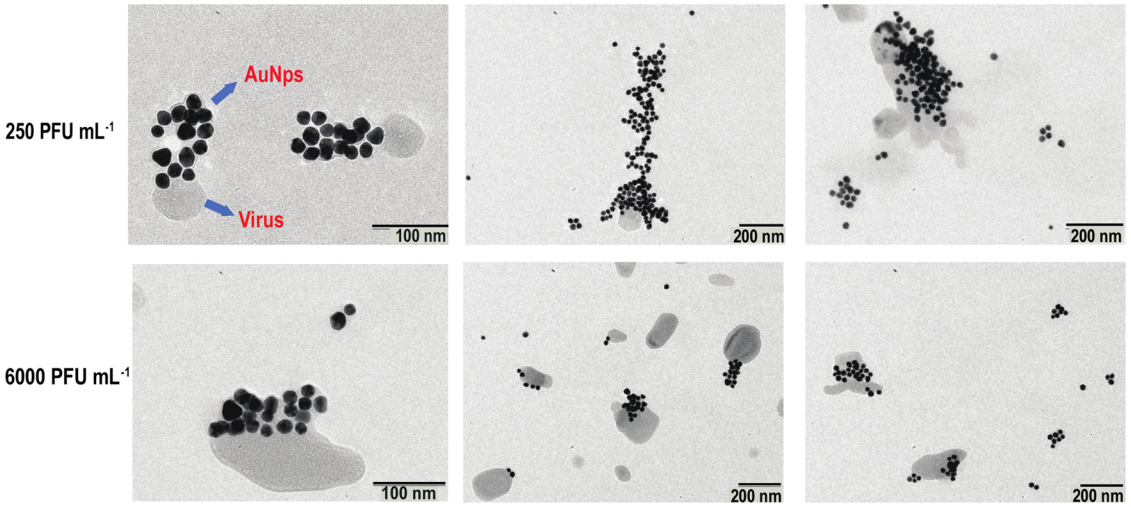


**Figure 2.** TEM micrographs of f-AuNPs after exposure to 250 and 6000 PFU $mL^{-1}$ of SARS-CoV-2.

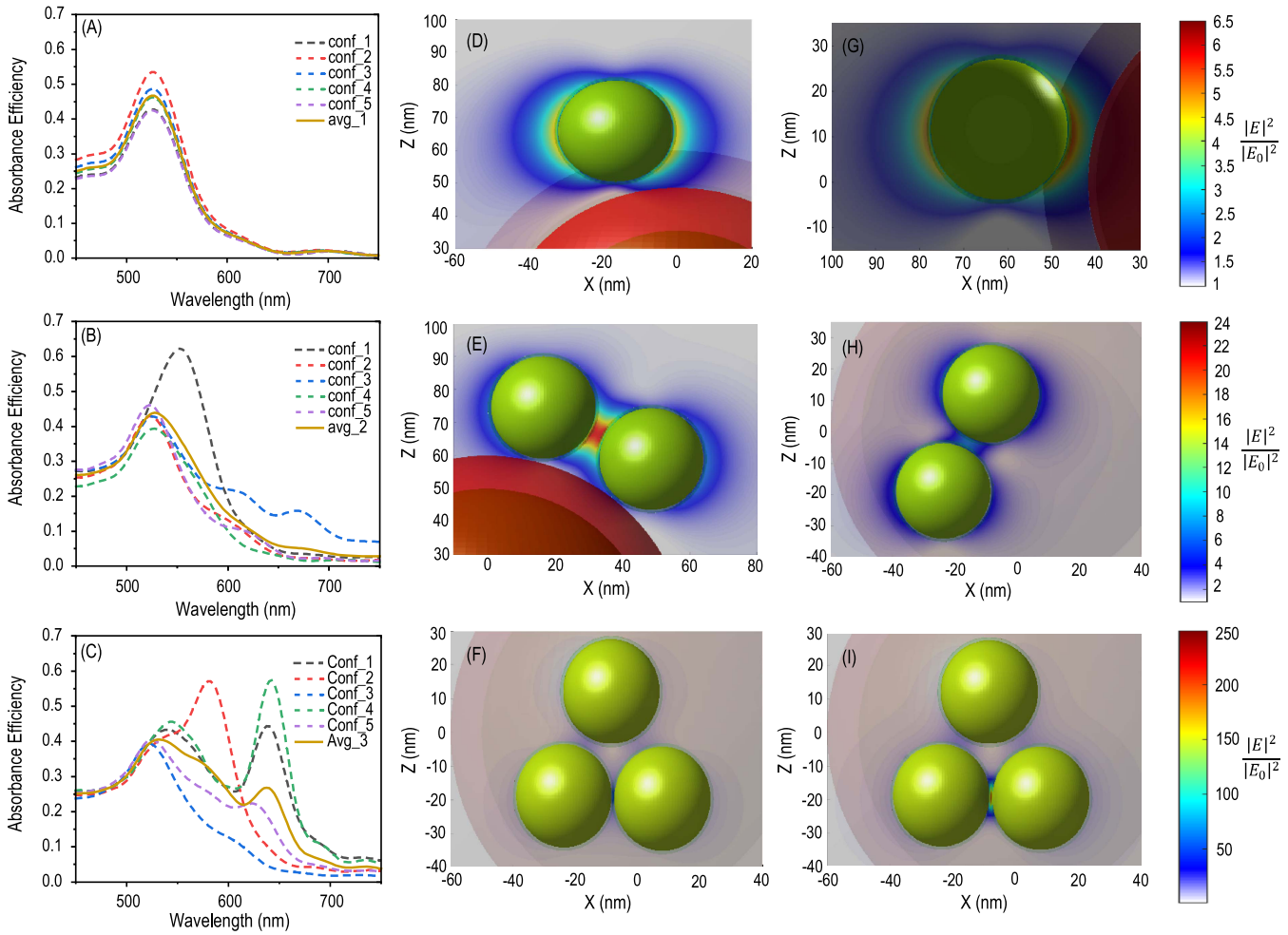


**Figure 3.** Spectral absorption efficiency for clusters with (A) one, (B) two, and (C) three f-AuNPs. (D) and (G) show the electric field amplitude at the resonant frequency for Conf_1 and Conf_2 in (A), respectively. (E) and (H) show the electric field amplitude at the resonant frequency for Conf_1 and Conf_4 in (B), respectively. (F) and (I) show the electric field amplitude at the wavelength resonant $\lambda$ = 545 nm and $\lambda$ = 642 nm for Conf_ 3 in (C).

attachment of antibodies was confirmed with the ATR spectra in Figure 1C, featuring O−H and C═O bands assigned to stretching vibrations of −COOH groups of Au−MUA[61] at 3261 and 1433 $cm^{-1}$, which are slightly altered after the addition of PEG. The 3261 $cm^{-1}$ band was increased, while the 1433 $cm^{-1}$ band almost disappeared after bioconjugation. The functionalization of AuNPs affected their $\zeta$-potential in Figure 1D, ranging from −43.96 mV for AuNPs to −35.32 mV after


https://doi.org/10.1021/acsami.2c15407
ACS Appl. Mater. Interfaces XXXX, XXX, XXX−XXX

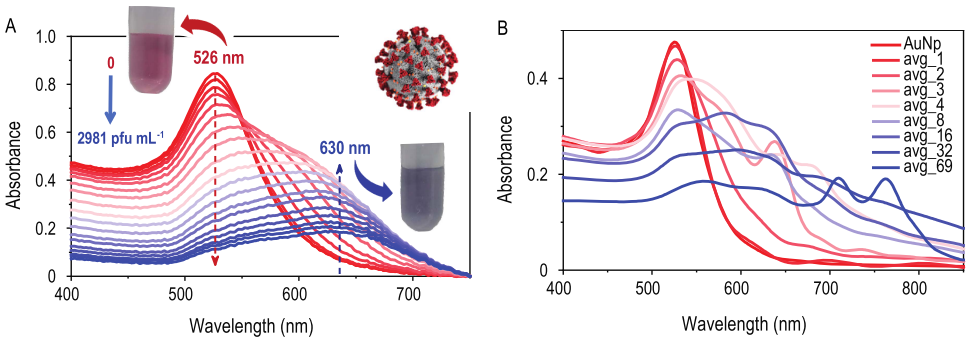


**Figure 4.** (A) UV−vis spectra for solutions containing inactivated SARS-CoV-2 virus at concentrations 0, 7, 144, 250, 418, 520, 636, 750, 860, 971, 1073, 1172, 1268, 1360, 1781, 2142, 2459, 2736, and 2980 PFU $mL^{-1}$. As the concentration increases, there is a change from a reddish to bluish color in the f-AuNP solution, which is indicated in the inset photos. We used two colors (red and blue) in the spectra to indicate this gradual change. (B) Averaged spectral absorption efficiency for various f-AuNPs in the aggregate clusters was obtained with FDTD simulations. The spectra are also shown in two colors to indicate the color change. The caption avg corresponds to the average spectral absorption efficiency of five different configurations in the FDTD simulations.

MUA coating. The $\zeta$-potential further varied by attaching PEG (−38.72 mV), antibodies (−31.64 mV), and BSA (−33.68 mV). When 2.0 $\mu$g $mL^{-1}$ SARS-CoV-2 S protein was added, the $\zeta$-potential decreased (in modulus) to −30.86 mV, as expected from the literature.[62] It is worth noting that BSA improves the stability of AuNPs functionalized with PEG and increases the $\zeta$-potential,[63] which decreases when f-AuNPs interact with the S protein of the SARS-CoV-2 virus.

TEM images of functionalized AuNPs (f-AuNPs) exposed to SARS-CoV-2 at 250 and 6000 PFU concentrations are shown in Figure 2. For both concentrations, clusters of different numbers of f-AuNPs are formed on the virus surface and may not cover the entire surface. For 250 PFU, AuNP clusters recover the viral particles as expected,[64] and several neighboring NPs agglomerate around it. The hydrodynamic radius of the AuNPs increases with the SARS-CoV-2 concentration,[65] as indicated in DLS measurements in Figure S3 in the Supporting Information. At 6000 PFU, some virus particles are not covered by AuNPs.

**3.2. Simulations.** The phenomenon of f-AuNP aggregation and clustering on the virus surface forms the basis of the colorimetric-based sensor proposed in this work. It is, therefore, useful to model such interactions with FDTD simulations, which allow one to analyze the light absorption properties of the f-AuNP−virus system as a function of interparticle distances and cluster sizes. Figure 3 shows the absorption efficiency spectra for aggregates with different numbers of f-AuNPs (1−3), including the spectrum for an isolated f-AuNP. Since the f-AuNPs are randomly located, a statistical study was necessary for which we employed five different AuNP configurations for a given cluster size, denoted with distinct captions (conf_1-conf_5). The caption avg corresponds to the average of these configurations. We plot the electric field amplitude at the resonant frequency for some configurations, with the same color map scale for some cluster sizes. The FDTD results in Figure 3A indicate that an isolated f-AuNP exhibits a strong LSPR around ∼525 nm, in agreement with the experimental spectrum in Figure 1B. The near-field electric distribution for the modified-AuNP at the plasmon resonance wavelength is shown in Figure S4 in the Supporting Information. Due to the LSPR effect, the electric field was enhanced around the f-AuNP, with the enhancement locally reaching up to 4.5 times the intensity of incident light.

On the other hand, when f-AuNP are aggregated on the virus surface, the spectrum of different configurations differs in absorption amplitude and frequency for maximum absorption from the isolated f-AuNP. In particular, as the f-AuNP and virus align with the polarization direction of the source ($x$-axis), the absorption amplitude, resonance frequency, and electromagnetic field in the region of contact increase (Figure 3D,G). Compared with the far-field response of an isolated f-AuNP, the changes are minimal, which is not helpful for colorimetric sensors. In contrast to the single nanoparticle−virus system, a new set of plasmonic modes are seen at larger wavelengths, with a significant enhancement of the electric field (especially in the gap between nanoparticles, *i.e.*, at the "hotspots"), for some dimer- or trimer-virus configurations (Figure 3B,C,E,F,H,I). These new bands arise from the strong near-field coupling of LSPRs of individual particles, which can be understood in terms of the plasmon hybridization theory.[66] From the field profiles, it could be inferred that plasmonic coupling decreases with an increase in interparticle separation. It is also possible to infer a strong dependence of the plasmonic coupling upon the relative orientations of the cluster concerning the polarization direction of the source. The more aligned the f-AuNPs with the incident electric field, the stronger the plasmonic coupling is. The absorption efficiency spectra for aggregates with nanoparticle numbers 4, 8, 16, and 32 are shown in Figure S5. As the size of the cluster increases for each random cluster configuration, there is an increase in the probability of matching the axis in a hotspot with the polarization light, which leads the optical absorption spectrum to shift toward larger wavelengths, with the appearance of new plasmonic bands. Since these variations are associated with intense color variations of the solutions, the theoretical results highlight the importance of aggregation and cluster formation of f-AuNPs on the virus surface in Figure 2. Hence, the larger the cluster, the easier it is to detect the virus.

**3.3. Spectrophotometric and Naked-Eye Detection.** A quantitative determination of inactivated SARS-CoV-2 and the Spike protein was performed with absorbance spectroscopy in artificial saliva samples. Figure S6A shows a decrease in the absorbance of the plasmonic band centered at 526 nm with increasing concentration. This decrease was expected because polyclonal antibodies may bind to the S protein at multiple epitopes so that the S protein serves as a crosslinker to aggregate f-AuNPs, thus quenching the plasmonic band.


https://doi.org/10.1021/acsami.2c15407
ACS Appl. Mater. Interfaces XXXX, XXX, XXX−XXX

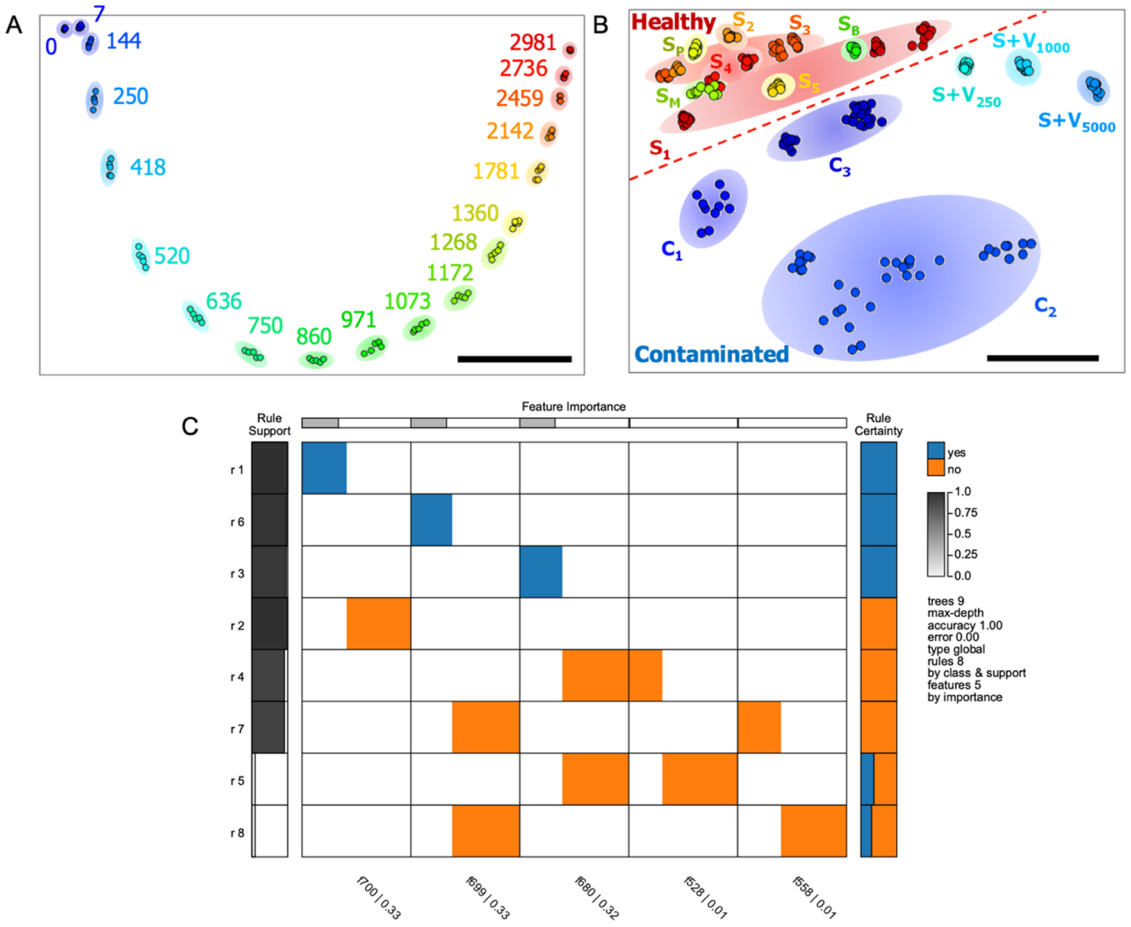


**Figure 5.** (A) IDMAP visualization of data from the response with the plasmonic biosensor for SARS-CoV-2 virus (concentrations between 7 PFU and 2981 PFU) diluted in 0.5 mmol $L^{-1}$ PBS (pH 7.4). (B) IDMAP visualization of the data for human saliva of healthy volunteers (with no symptoms, but not tested) ($S_1$−$S_5$), $S_p$ and $S_m$ (volunteers with no symptoms and who were tested negative for Covid-19), $S_B$ Saliva diluted in 0.5 mmol $L^{-1}$ PBS (pH 7.4), human saliva from volunteers tested negative (S) contaminated with 250, 1000, and 5000 PFU and positive PCR test of virus-carrying patients ($C_1$, $C_2$, and $C_3$). (C) ExMatrix representation using the RF model (9 Decision Trees−8 logic rules) for the binary problem, with YES or NO classes for positive and negative SARS-COV-2 patients, respectively.

Indeed, quenching of f-AuNPs was reported for other analytes,[67] depending on the type of coupling, interparticle spacing, and local dielectric environment.[67] No other band is formed since the Spike protein is small compared to the virus. The protein reacts with the antibody on the f-AuNP surface, and no clusters of f-AuNPs are formed. Hence, there are only refractive index changes, which can only be detected at high concentrations of SARS-CoV-2.[68] In contrast, for the inactivated SARS-CoV-2, Figure 4A shows that the plasmonic band is redshifted with the concentration, and another band appears at 636 nm. This new band results from the large clusters of f-AuNPs on the virus surface, as discussed in Section 3.2, and leads to a change in the solution color from red (w/o virus) to blue (w/ virus). This is represented by changing the color of the spectra in Figure 4A. The limit of detection (LOD) was calculated from the parameters extracted by fitting the experimental results using the Langmuir−Hill model for the inactivated virus (Figure S7). LOD is 0.28 PFU $mL^{-1}$ by taking the peak shift ($\Delta\lambda$) from normalized spectra and 0.29 PFU $mL^{-1}$ using the absorbance ratio at 526 and 636 nm ($A_{526}/A_{636}$).

Figure 4B shows theoretical spectra that resemble the experimental spectra in Figure 4A. To interpret the spectra, we recall the theoretical calculations in Figure 3 (and Figure 5S in the Supporting Information), where the average absorption efficiency was calculated for clusters with 1, 2, 3, 4, 8, 16, and 32 NPs and for the case in which the virus surface is entirely covered by f-AuNPs (*i.e.*, with 69 NPs). Comparing with the theoretical results in Figure 4B, we infer that the absorption band centered at 526 nm is mainly related to the absorption response of isolated AuNPs, which are dominant at low concentrations. The plasmonic response of the single nanoparticle−virus system and the transversal plasmonic couplings in larger aggregates could also contribute to the appearance of this band. On the other hand, as the virus concentration increases, the f-AuNPs agglomerate on the virus surface to form clusters of different sizes. Since these clusters exhibit different optical responses, the plasmonic band becomes broader. It should be noted that the predicted bands with FDTD for complete virus coverage with f-AuNPs are not observed experimentally. Therefore, the probability of experimentally observing total virus coverage is small, consistent with the SEM images in Figure 2.

Despite the evident changes in color, choosing one specific wavelength to collect absorbance values from hundreds of absorbance spectra is difficult. To facilitate interpretation by the reader, we used a multidimensional projection technique, referred to as Interactive Document Mapping (IDMAP).[69]


https://doi.org/10.1021/acsami.2c15407
ACS Appl. Mater. Interfaces XXXX, XXX, XXX−XXX

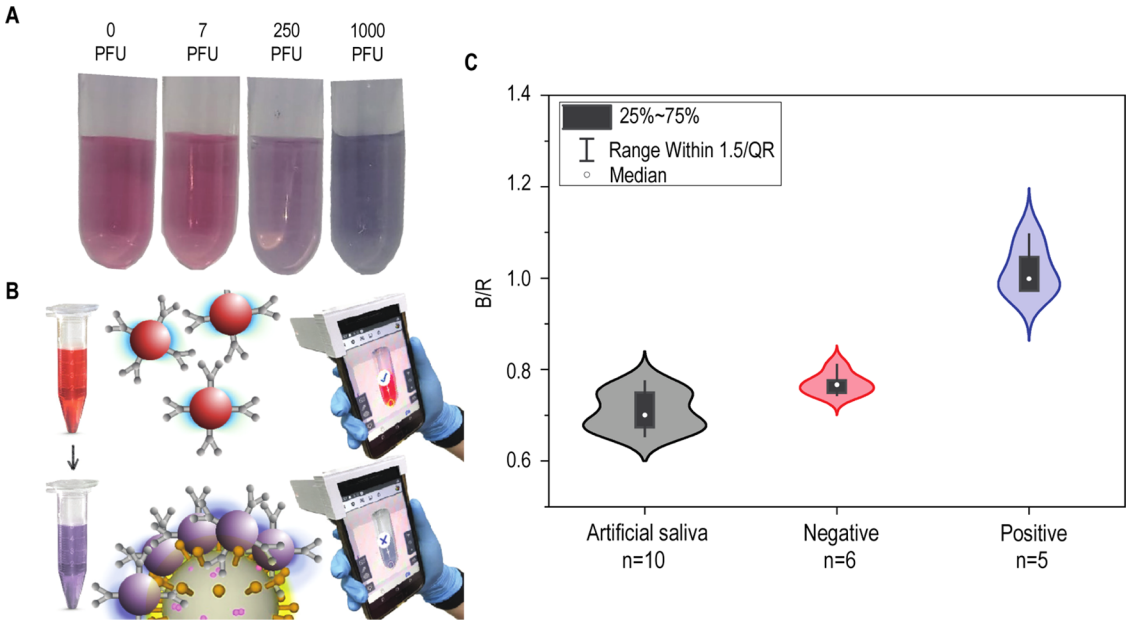


**Figure 6.** (A) Photo shows the colorimetric response of the plasmonic biosensor for different concentrations of inactivated SARS-CoV-2 in 0.5 mmol $L^{-1}$ PBS, pH 7.4. (B) Schematic design for SARS-CoV-2 virus detection with a smartphone camera. (C) Violin plots for the colorimetric results from the SARS-CoV-2 analysis in saliva samples using the biosensor.

The FastMap method was used to reduce the 350 dimensions, *i.e.*, the UV−vis spectrum (400−750 nm), to only 2 dimensions.[69] Hence, one converts each spectrum into a single-colored dot on the visualization map. Evident discrimination of the samples with distinct concentrations of inactivated virus, from 0 to 2981 PFU $mL^{-1}$, is obtained in Figure 5A, with a silhouette coefficient of 0.97 (which varies from −1 to 1).[69] To demonstrate the applicability of the f-AuNPs biosensor, we analyzed several saliva samples (in triplicate, $n = 3$) obtained from 10 volunteers as follows: five healthy volunteers ($S_1$−$S_5$) who were not tested; two volunteers with negative PCR tests ($S_P$ and $S_M$), three volunteers tested positive for Covid-19 ($C_1$, $C_2$, and $C_3$). Also, the saliva samples of one of the volunteers who tested negative were diluted in 0.5 mmol $L^{-1}$ PBS (samples $S_B$) and then spiked with the inactivated virus at 250, 1000, and 5000 PFU $mL^{-1}$. There were, therefore, 14 distinct types of samples whose spectra were projected in the IDMAP plot in Figure 5B. There is a clear separation of samples from healthy individuals on the left-upper side of the map (reddish dots), while the saliva samples from contaminated patients and healthy individuals spiked with standards of 250 to 5000 PFU $mL^{-1}$ are located on the bottom of the map (bluish dots). Diagnosis of COVID-19 could also be made with the data from the saliva samples using supervised machine learning within the multidimensional calibration space concept.[70] An accuracy of 100% was obtained in the binary classification (YES or NO for the virus) when the random forest (RF) algorithm was applied. The results are illustrated in the Explainable Matrix (ExMatrix) representation[70] in Figure 5C. The space had five dimensions, *i.e.*, light absorption at five frequencies had to be used in the eight rules of the RF algorithm. It is also significant that the first three dimensions were already responsible for 98% of the information.

**3.4. Interferents and Other Applications.** To assess the selectivity of the proposed plasmonic biosensor, proteins of different viruses were chosen as interferents, including SARS, H1N1, and Dengue, at concentrations of $2 \times 10^{-6}$ and $2 \times 10^{-4}$ $\mu g\ mL^{-1}$ in PBS. These data were projected in Figure S8 (Supporting Information) with SARS-CoV-2 in concentrations between 7 and 2981 PFU $mL^{-1}$, with the interferents being grouped around the data for low concentrations of the SARS-CoV-2 virus. High (0.4−5.6 $\mu g\ mL^{-1}$) and low concentrations ($2 \times 10^{-6}$ and $2 \times 10^{-4}$ $\mu g\ mL^{-1}$) of Spike protein were also projected with interferents to demonstrate how different the proteins are from the viruses since they are placed in opposite directions as depicted in the IDMAP plot of Figure S9.

The impact of the exposure of virus particles from biological aerosols on sewage workers, communities, and wildlife should be investigated, along with initiatives to reduce the load of viruses in water reservoirs.[16] This type of monitoring requires simple methods for detecting and quantifying SARS-CoV-2 in waters (and wastewaters), mainly to identify possible routes of SARS-CoV-2 into water bodies.[71] This work demonstrates that the plasmonic biosensor can be applied in complex matrices. We tested river water (without a precleaning step) samples spiked with inactivated SARS-CoV-2 virus at five concentrations (7, 250, 1000, 5000, and 6000 PFU $mL^{-1}$). The separation in Figure S10 for these data indicates that the plasmonic biosensor can also be employed in environmental monitoring for the presence of SARS-CoV-2.

**3.5. Smartphone-Based Detection.** A rapid, inexpensive, and label-free method for real-time detection of SARS-CoV-2 was developed based on the surface plasmon resonance of f-AuNPs utilizing a smartphone application, Color Grab (see Figure S11 in the Supporting Information). A redshift in the absorbance of colloidal AuNPs is observed with saliva samples in the absence of the virus; when the inactivated virus is added, as shown in Figure 6A, a color change from red to blue is observed, as expected from the literature.[31,40] Figure S12 shows a blue color predominating for high PFU concentrations (*i.e.*, >2000 PFU $mL^{-1}$). These color differences can be distinguished with the naked eye by humans with normal trichromatic vision who can combine in their brain three


https://doi.org/10.1021/acsami.2c15407
ACS Appl. Mater. Interfaces XXXX, XXX, XXX−XXX

Table 1. Analytical Performance of the Optical Biosensor Using the Digital Image Analysis of the Ratio of Blue-to-Red (B/R) Channels in Different Sample Media

| assay | medium | analytical measurement | linear range ($n$ = 5, PFU mL$^{-1}$) | intercept | slope | $R^2$ | LOD |
|---|---|---|---|---|---|---|---|
| A | buffer | B/R | 7−2000 | −0.124 | 0.169 | 0.997 | 2.2 |
| B | saliva | B/R | 250−5000 | −0.411 | 0.170 | 0.903 | 2.0 |
| C | river | B/R | 7−2000 | −0.098 | 0.156 | 0.941 | 3.4 |

independent wavelengths, corresponding to red, green, and blue, to generate the color observed.[72] However, the perception of color differences is not the same in all individuals, and many users may suffer from problems such as color blindness or color vision deficiency.[72] Furthermore, these devices may be affected by environmental conditions (*e.g.*, poor ambient lighting or flashing lights of emergency vehicles) in addition to natural, person-to-person perceptual differences. These limitations can be mitigated with image processing,[72] as we have done here. We employed the RGB model, where each component of the color space may vary between 0 and 255 in images obtained under controlled ambient light with a simple box for photography and accessories to hold a smartphone (Figure S11). Figure 6B shows an illustration of the result displayed on a smartphone. The results from the color analysis on the digital images are given in the violin plot[73] of Figure 6C, featuring data from artificial saliva and saliva of healthy donors and patients.

Using color Grab and RGB values from the images taken with a smartphone camera, the absorbance ratio (blue/red) was calculated to quantify the concentration of SARS-CoV-2 virus as in ref 73. Since the application Color Grab is unavailable on some smartphones, we tested a different approach for digital image analysis with a free, open-source image processing software (ImageJ) to obtain the RGB values. One-way analysis of variance (ANOVA) followed by Tukey's test performed at low, medium, and high SARS-CoV-2 concentrations showed no significant differences ($p < 0.05$) between the images treated with a smartphone app and ImageJ. The detection limit was estimated as described by the International Union of Pure and Applied Chemistry (IUPAC).[18] Table 1 shows the analytical parameters for three types of assays. The first one was performed in PBS with increasing concentrations of inactivated virus (assay A), leading to a LOD of 2.2 PFU mL$^{-1}$. In Assay B, the saliva samples from a volunteer with a negative PCR test were spiked with the inactivated virus at concentrations from 250 to 5000 PFU mL$^{-1}$. The LOD obtained from the digital image analysis was 2.0 PFU mL$^{-1}$. Assay C was conducted with samples collected from river water samples without a precleaning step. These samples were spiked with inactivated virus from 7 to 2000 PFU mL$^{-1}$ (see Figure S14 in the Supporting Information), and a LOD of 3.4 PFU mL$^{-1}$ was obtained for the digital image analysis. It is also worth mentioning that the images from human saliva samples spiked with H1N1 and dengue virus proteins could not be distinguished from those of healthy volunteers.

## 4. CONCLUSIONS

The approach of functionalizing Au nanoparticles (f-AuNPs) with polyclonal antibodies for SARS-CoV-2 was exploited in plasmonic biosensors to detect inactivated viruses with a colorimetric, instrument-free technique. The sensitivity is sufficient for diagnosis using saliva, with a limit of detection (LOD) of 2.2 and 2.0 PFU mL$^{-1}$ in assays with the inactivated virus in PBS solutions and the saliva of a volunteer, respectively. We found that the high sensitivity is related to the processes involving the cluster formation of f-AuNPs around the virus. As indicated in the FDTD computer simulations, a significant color change is only observed when large clusters are formed. The suitability of the biosensor with f-AuNPs was confirmed with other detection principles, including UV−vis spectroscopy and dynamic light scattering. The plasmonic biosensor specific for SARS-CoV-2 was demonstrated in experiments with potential interferents, such as the proteins from SARS, H1N1, and Dengue viruses. Detection of the UV-inactivated SARS-CoV-2 in human saliva and river waters could be done within 5 min, as the liquid and solutions changed color from red to purple, with possible observation with naked eyes. This color change was exploited in a smartphone application where images taken with the smartphone camera were processed with Color Grab and ImageJ software. With the latter, it was possible to determine whether the sample was positive for SARS-CoV-2 and to estimate the virus concentration. The app may also incorporate image processing combined with machine learning to provide COVID-19 diagnosis, whose accuracy in the tests performed with the colorimetric assay was 100%. These results indicate that plasmonic biosensors, like those developed here, can be used for low-cost COVID-19 diagnosis and monitoring within the point-of-care paradigm and in poor or remote locations.

Moreover, it is critical to consider the probability of environmental contamination and spread through wastewater and river waters. For example, places with poor sanitation and inadequate treatment can lead to nonpoint contamination of surface waters with SARS-CoV-2. For this reason, investigating methodologies that allow the detection of pathogens in places with little infrastructure is essential. Our proposed biosensor is promising for using river water samples without any previous treatment.

## ■ ASSOCIATED CONTENT

### Supporting Information

The Supporting Information is available free of charge at https://pubs.acs.org/doi/10.1021/acsami.2c15407.

Microscopy analysis; DLS results; FDTD simulation; UV−vis spectra; IDMAP plot; pictures of colorimetric samples and device; and comparison of main contributions from the literature (PDF)

## ■ AUTHOR INFORMATION

### Corresponding Author

**Elsa M. Materón** − *São Carlos Institute of Physics, University of São Paulo, 13560-970 São Carlos, SP, Brazil; Instituto de Química de São Carlos, Universidade de São Paulo, 13566-590 São Carlos, SP, Brazil;* orcid.org/0000-0002-3382-1193; Email: elsa_materon@yahoo.com



https://doi.org/10.1021/acsami.2c15407
ACS Appl. Mater. Interfaces XXXX, XXX, XXX−XXX

## Authors

**Faustino R. Gómez** − *São Carlos Institute of Physics, University of São Paulo, 13560-970 São Carlos, SP, Brazil;* orcid.org/0000-0001-5758-0489

**Mariana B. Almeida** − *Instituto de Química de São Carlos, Universidade de São Paulo, 13566-590 São Carlos, SP, Brazil; Instituto Nacional de Ciência e Tecnologia de Bioanalítica-INCTBio, 13083-970 Campinas, SP, Brazil*

**Flavio M. Shimizu** − *Department of Applied Physics, "Gleb Wataghin" Institute of Physics (IFGW), University of Campinas (UNICAMP), 13083-859 Campinas, SP, Brazil;* orcid.org/0000-0002-4833-9893

**Ademar Wong** − *Department of Chemistry, Federal University of São Carlos (UFSCar), 13560-970 São Carlos, São Paulo, Brazil*

**Kelcilene B. R. Teodoro** − *Nanotechnology National Laboratory for Agriculture, Embrapa Instrumentation, 13560-970 São Carlos, SP, Brazil;* orcid.org/0000-0003-4337-4849

**Filipe S. R. Silva** − *Instituto de Química de São Carlos, Universidade de São Paulo, 13566-590 São Carlos, SP, Brazil;* orcid.org/0000-0003-3085-8510

**Manoel J. A. Lima** − *Instituto de Química de São Carlos, Universidade de São Paulo, 13566-590 São Carlos, SP, Brazil*

**Monara Kaelle S. C. Angelim** − *Department of Genetics Evolution, Microbiology, and Immunology, Institute of Biology, University of Campinas, 13083-970 Campinas, SP, Brazil*

**Matias E. Melendez** − *Molecular Carcinogenesis Program, National Cancer Institute, 20231-050 Rio de Janeiro, RJ, Brazil;* orcid.org/0000-0002-0643-6185

**Nelson Porras** − *Physics Department, del Valle University, AA 25360 Cali, Colombia*

**Pedro M. Vieira** − *Department of Genetics Evolution, Microbiology, and Immunology, Institute of Biology, University of Campinas, 13083-970 Campinas, SP, Brazil*

**Daniel S. Correa** − *Nanotechnology National Laboratory for Agriculture, Embrapa Instrumentation, 13560-970 São Carlos, SP, Brazil;* orcid.org/0000-0002-5592-0627

**Emanuel Carrilho** − *Instituto de Química de São Carlos, Universidade de São Paulo, 13566-590 São Carlos, SP, Brazil; Instituto Nacional de Ciência e Tecnologia de Bioanalítica-INCTBio, 13083-970 Campinas, SP, Brazil;* orcid.org/0000-0001-7351-8220

**Osvaldo N. Oliveira, Jr.** − *São Carlos Institute of Physics, University of São Paulo, 13560-970 São Carlos, SP, Brazil;* orcid.org/0000-0002-5399-5860

**Ricardo B. Azevedo** − *Laboratory of Nanobiotechnology, Department of Genetics and Morphology, Institute of Biological Sciences, University of Brasilia, 70910-900 Brasilia, DF, Brazil*

**Débora Goncalves** − *São Carlos Institute of Physics, University of São Paulo, 13560-970 São Carlos, SP, Brazil*

Complete contact information is available at: https://pubs.acs.org/10.1021/acsami.2c15407


## Author Contributions

E.M.M.: Methodology, investigation, acquisition of photos using a smartphone, synthesis of gold nanoparticles, validation, conceptualization, project administration, data analysis, visualization, writing for the original draft, and editing. F.R.G.: Conceptualization, acquisition of photos with a smartphone, simulations, visualization, writing for the original draft, and editing. M.B.A.: Discussion of results of the images, visualization, and writing for the original draft. F.M.S.: artificial saliva methodology, discussion of results, data curation, visualization, writing for the original draft, and editing. A.W.: Synthesis of gold nanoparticles, collecting river samples, discussion of results, writing for the original draft, and editing. K.B.R.T. and D.S.C.: Investigation with DLS analysis, validation, and writing for the original draft. F.S.R.S.: protein quantification, acquisition of photos with a smartphone, validation, and writing for the original draft. M.J.A.L.: Discussion of image results, 3D printed box design and printing, and writing for the original draft. M.K.S.C.A., M.E.M., and P.M.V.: inactivation of virus and discussion of results and writing for the original draft. N.P.: funding, computer simulations, and discussion of theoretical simulations. E.C.: Supervision, funding, saliva samples, writing for the original draft, and editing. O.N.O.Jr., R.B.A., and D.G.: Supervision, funding, project administration, writing for the original draft, and editing. All of the authors discussed the results and edited/reviewed the manuscript.

## Notes

The authors declare no competing financial interest.

The authors declare that they have no known competing financial interests or personal relationships that could have appeared to influence the work reported in this paper.

## ■ ACKNOWLEDGMENTS

This work was supported by CAPES (Finance code 001), INEO, CNPq (402816/2020-0, 304431/2020-6, 311757/2019-7, 465389/2014-7, 115857/2022-2), and FAPESP (2018/22214-6, 2014/50867-3, 2019/19235-4, 2021/08387-8, 2017/03879-4), Edital de projetos integrados de pesquisa em áreas estratégicas (PIPAE).

## ■ REFERENCES

(1) Malekshahi, A.; Khanizadeh, S.; Fallahi, S.; Talei, G.; Birjandi, M.; Hajizadeh, F. Diagnostic Power of One-Step and Two-Step RT-QPCR Methods to SARS-CoV-2 Detection. *BMC Infect. Dis.* **2022**, *22*, No. 505.

(2) Bruzzone, B.; De Pace, V.; Caligiuri, P.; Ricucci, V.; Guarona, G.; Pennati, B. M.; Boccotti, S.; Orsi, A.; Domnich, A.; Da Rin, G.; Icardi, G. Comparative Diagnostic Performance of Rapid Antigen Detection Tests for COVID-19 in a Hospital Setting. *Int. J. Infect. Dis.* **2021**, *107*, 215−218.

(3) Kendall, E. A.; Arinaminpathy, N.; Sacks, J. A.; Manabe, Y. C.; Dittrich, S.; Schumacher, S. G.; Dowdy, D. W. Antigen-Based Rapid Diagnostic Testing or Alternatives for Diagnosis of Symptomatic COVID-19: A Simulation-Based Net Benefit Analysis. *Epidemiology* **2021**, *32*, 811−819.

(4) Warsi, I.; Khurshid, Z.; Shazam, H.; Umer, M. F.; Imran, E.; Khan, M. O.; Slowey, P. D.; Goodson, J. M. Saliva Exhibits High Sensitivity and Specificity for the Detection of SARS-COV-2. *Diseases* **2021**, *9*, 38.

(5) Wyllie, A. L.; Fournier, J.; Casanovas-Massana, A.; Campbell, M.; Tokuyama, M.; Vijayakumar, P.; Warren, J. L.; Geng, B.; Muenker, M. C.; Moore, A. J.; Vogels, C. B. F.; Petrone, M. E.; Ott, I. M.; Lu, P.; Venkataraman, A.; Lu-Culligan, A.; Klein, J.; Earnest, R.; Simonov, M.; Datta, R.; Handoko, R.; Naushad, N.; Sewanan, L. R.; Valdez, J.; White, E. B.; Lapidus, S.; Kalinich, C. C.; Jiang, X.; Kim, D. J.; Kudo, E.; Linehan, M.; Mao, T.; Moriyama, M.; Oh, J. E.; Park, A.; Silva, J.; Song, E.; Takahashi, T.; Taura, M.; Weizman, O.-E.; Wong, P.; Yang, Y.; Bermejo, S.; Odio, C. D.; Omer, S. B.; Dela Cruz, C. S.; Farhadian, S.; Martinello, R. A.; Iwasaki, A.; Grubaugh, N. D.; Ko, A. I. Saliva or Nasopharyngeal Swab Specimens for Detection of SARS-CoV-2. *N. Engl. J. Med.* **2020**, *383*, 1283−1286.

(6) Bulfoni, M.; Sozio, E.; Marcon, B.; De Martino, M.; Cesselli, D.; De Carlo, C.; Martinella, R.; Migotti, A.; Vania, E.; Zanus-Fortes, A.; De Piero, J.; Nencioni, E.; Tascini, C.; Isola, M.; Curcio, F. Validation of a Saliva-Based Test for the Molecular Diagnosis of SARS-CoV-2 Infection. *Dis. Markers* **2022**, *2022*, 1−8.
(7) de Oliveira, C. M.; Brochi, L.; Scarpelli, L. C.; Lopes, A. C. W.; Levi, J. E. SARS-CoV-2 Saliva Testing Is a Useful Tool for Covid-19 Diagnosis. *J. Virol. Methods* **2021**, *296*, 114241.
(8) Bustos-Garcia, B.; Garza-Manero, S.; Cano-Dominguez, N.; Lopez-Sanchez, D. M.; Salgado-Montes de Oca, G.; Salgado-Aguayo, A.; Recillas-Targa, F.; Avila-Rios, S.; Valdes, V. J. Development and Testing of a Low-Cost Inactivation Buffer That Allows for Direct SARS-CoV-2 Detection in Saliva. *Vaccines* **2022**, *10*, 730.
(9) Lin, Y. C.; Malott, R. J.; Ward, L.; Kiplagat, L.; Pabbaraju, K.; Gill, K.; Berenger, B. M.; Hu, J.; Fonseca, K.; Noyce, R. S.; Louie, T.; Evans, D. H.; Conly, J. M. Detection and Quantification of Infectious Severe Acute Respiratory Coronavirus-2 in Diverse Clinical and Environmental Samples. *Sci. Rep.* **2022**, *12*, No. 5418.
(10) Sender, R.; Bar-On, Y. M.; Gleizer, S.; Bernshtein, B.; Flamholz, A.; Phillips, R.; Milo, R. The Total Number and Mass of SARS-CoV-2 Virions. *Proc. Natl. Acad. Sci. U.S.A.* **2021**, *118*, No. e2024815118.
(11) Johnson, T. J.; Nishida, R. T.; Sonpar, A. P.; Lin, Y. C. J.; Watson, K. A.; Smith, S. W.; Conly, J. M.; Evans, D. H.; Olfert, J. S. Viral Load of SARS-CoV-2 in Droplets and Bioaerosols Directly Captured during Breathing, Speaking and Coughing. *Sci. Rep.* **2022**, *12*, No. 3484.
(12) Bradburne, A. F.; Bynoe, M. L.; Tyrrell, D. A. J. Effects of a "New" Human Respiratory Virus in Volunteers. *Br. Med. J.* **1967**, *3*, 767−769.
(13) Tran, H. N.; Le, G. T.; Nguyen, D. T.; Juang, R.; Rinklebe, J.; Bhatnagar, A.; Lima, E. C.; Iqbal, H. M. N.; Sarmah, A. K.; Chao, H.-P. SARS-CoV-2 Coronavirus in Water and Wastewater: A Critical Review about Presence and Concern. *Environ. Res.* **2021**, *193*, No. 110265.
(14) de Oliveira, L. C.; Torres-Franco, A. F.; Lopes, B. C.; da Silva Santos, B. S. Á.; Costa, E. A.; Costa, M. S.; Reis, M. T. P.; Melo, M. C.; Polizzi, R. B.; Teixeira, M. M.; Mota, C. R. Viability of SARS-CoV-2 in River Water and Wastewater at Different Temperatures and Solids Content. *Water Res.* **2021**, *195*, No. 117002.
(15) Haramoto, E.; Malla, B.; Thakali, O.; Kitajima, M. First Environmental Surveillance for the Presence of SARS-CoV-2 RNA in Wastewater and River Water in Japan. *Sci. Total Environ.* **2020**, *737*, No. 140405.
(16) Bivins, A.; Greaves, J.; Fischer, R.; Yinda, K. C.; Ahmed, W.; Kitajima, M.; Munster, V. J.; Bibby, K. Persistence of SARS-CoV-2 in Water and Wastewater. *Environ. Sci. Technol. Lett.* **2020**, *7*, 937−942.
(17) Rashed, M. Z.; Kopechek, J. A.; Priddy, M. C.; Hamorsky, K. T.; Palmer, K. E.; Mittal, N.; Valdez, J.; Flynn, J.; Williams, S. J. Rapid Detection of SARS-CoV-2 Antibodies Using Electrochemical Impedance-Based Detector. *Biosens. Bioelectron.* **2021**, *171*, No. 112709.
(18) Fabiani, L.; Saroglia, M.; Galatà, G.; De Santis, R.; Fillo, S.; Luca, V.; Faggioni, G.; D'Amore, N.; Regalbuto, E.; Salvatori, P.; Terova, G.; Moscone, D.; Lista, F.; Arduini, F. Magnetic Beads Combined with Carbon Black-Based Screen-Printed Electrodes for COVID-19: A Reliable and Miniaturized Electrochemical Immunosensor for SARS-CoV-2 Detection in Saliva. *Biosens. Bioelectron.* **2021**, *171*, No. 112686.
(19) Saatçi, E.; Natarajan, S. State-of-the-Art Colloidal Particles and Unique Interfaces-Based SARS-CoV-2 Detection Methods and COVID-19 Diagnosis. *Curr. Opin. Colloid Interface Sci.* **2021**, *55*, No. 101469.
(20) Lau, C. S.; Aw, T.-C. SARS-CoV-2 Antigen Testing Intervals: Twice or Thrice a Week? *Diagnostics* **2022**, *12*, 1039.
(21) Amaral, C.; Antunes, W.; Moe, E.; Duarte, A. G.; Lima, L. M. P.; Santos, C.; Gomes, I. L.; Afonso, G. S.; Vieira, R.; Teles, H. S. S.; Reis, M. S.; da Silva, M. A. R.; Henriques, A. M.; Fevereiro, M.; Ventura, M. R.; Serrano, M.; Pimentel, C. A Molecular Test Based on RT-LAMP for Rapid, Sensitive and Inexpensive Colorimetric Detection of SARS-CoV-2 in Clinical Samples. *Sci. Rep.* **2021**, *11*, No. 16430.
(22) Xu, N.; Jin, S.; Wang, L. Metal Nanoparticles-Based Nanoplatforms for Colorimetric Sensing: A Review. *Rev. Anal. Chem.* **2021**, *40*, 1−11.
(23) Liang, P.; Guo, Q.; Zhao, T.; Wen, C. Y.; Tian, Z.; Shang, Y.; Xing, J.; Jiang, Y.; Zeng, J. Ag Nanoparticles with Ultrathin Au Shell-Based Lateral Flow Immunoassay for Colorimetric and SERS Dual-Mode Detection of SARS-CoV-2 IgG. *Anal. Chem.* **2022**, *94*, 8466−8473.
(24) Ventura, B. D.; Cennamo, M.; Minopoli, A.; Campanile, R.; Censi, S. B.; Terracciano, D.; Portella, G.; Velotta, R. Colorimetric Test for Fast Detection of SARS-COV-2 in Nasal and Throat Swabs. *ACS Sens.* **2020**, *5*, 3043−3048.
(25) Han, H.; Wang, C.; Yang, X.; Zheng, S.; Cheng, X.; Liu, Z.; Zhao, B.; Xiao, R. Rapid Field Determination of SARS-CoV-2 by a Colorimetric and Fluorescent Dual-Functional Lateral Flow Immunoassay Biosensor. *Sens. Actuators, B* **2022**, *351*, No. 130897.
(26) Yadav, S.; Sadique, M. A.; Ranjan, P.; Kumar, N.; Singhal, A.; Srivastava, A. K.; Khan, R. Sers Based Lateral Flow Immunoassay for Point-of-Care Detection of Sars-Cov-2 in Clinical Samples. *ACS Appl. Bio Mater.* **2021**, *4*, 2974−2995.
(27) Georgiou, P. G.; Guy, C. S.; Hasan, M.; Ahmad, A.; Richards, S. J.; Baker, A. N.; Thakkar, N. V.; Walker, M.; Pandey, S.; Anderson, N. R.; Grammatopoulos, D.; Gibson, M. I. Plasmonic Detection of SARS-CoV-2 Spike Protein with Polymer-Stabilized Glycosylated Gold Nanorods. *ACS Macro Lett.* **2022**, *11*, 317−322.
(28) Antiochia, R. Nanobiosensors as New Diagnostic Tools for SARS, MERS and COVID-19: From Past to Perspectives. *Microchim. Acta* **2020**, *187*, No. 639.
(29) Lew, T. T. S.; Aung, K. M. M.; Ow, S. Y.; Amrun, S. N.; Sutarlie, L.; Ng, L. F. P.; Su, X. Epitope-Functionalized Gold Nanoparticles for Rapid and Selective Detection of SARS-CoV-2 IgG Antibodies. *ACS Nano* **2021**, *15*, 12286−12297.
(30) Huang, X.; Jain, P. K.; El-Sayed, I. H.; El-Sayed, M. A. Gold Nanoparticles: Interesting Optical Properties and Recent Applications in Cancer Diagnostics and Therapy. *Nanomedicine* **2007**, *2*, 681−693.
(31) Draz, M. S.; Shafiee, H. Applications of Gold Nanoparticles in Virus Detection. *Theranostics* **2018**, *8*, 1985−2017.
(32) Hall, W. P.; Ngatia, S. N.; Van Duyne, R. P. LSPR Biosensor Signal Enhancement Using Nanoparticle-Antibody Conjugates. *J. Phys. Chem. C* **2011**, *115*, 1410−1414.
(33) Mayer, K. M.; Hafner, J. H. Localized Surface Plasmon Resonance Sensors. *Chem. Rev.* **2011**, *111*, 3828−3857.
(34) Li, M.; Cushing, S. K.; Wu, N. Plasmon-Enhanced Optical Sensors: A Review. *Analyst* **2015**, *140*, 386−406.
(35) Pramanik, A.; Gao, Y.; Patibandla, S.; Mitra, D.; McCandless, M. G.; Fassero, L. A.; Gates, K.; Tandon, R.; Chandra Ray, P. The Rapid Diagnosis and Effective Inhibition of Coronavirus Using Spike Antibody Attached Gold Nanoparticles. *Nanoscale Adv.* **2021**, *3*, 1588−1596.
(36) Herizchi, R.; Abbasi, E.; Milani, M.; Akbarzadeh, A. Current Methods for Synthesis of Gold Nanoparticles. *Artif. Cells, Nanomed., Biotechnol.* **2016**, *44*, 596−602.
(37) Patterson, E. I.; Prince, T.; Anderson, E. R.; Casas-Sanchez, A.; Smith, S. L.; Cansado-Utrilla, C.; Solomon, T.; Griffiths, M. J.; Acosta-Serrano, Á.; Turtle, L.; Hughes, G. L. Methods of Inactivation of SARS-CoV-2 for Downstream Biological Assays. *J. Infect. Dis.* **2020**, *222*, 1462−1467.
(38) Lo, C. W.; Matsuura, R.; Iimura, K.; Wada, S.; Shinjo, A.; Benno, Y.; Nakagawa, M.; Takei, M.; Aida, Y. UVC Disinfects SARS-CoV-2 by Induction of Viral Genome Damage without Apparent Effects on Viral Morphology and Proteins. *Sci. Rep.* **2021**, *11*, No. 13804.
(39) Loveday, E. K.; Hain, K. S.; Kochetkova, I.; Hedges, J. F.; Robison, A.; Snyder, D. T.; Brumfield, S. K.; Young, M. J.; Jutila, M. A.; Chang, C. B.; Taylor, M. P. Effect of Inactivation Methods on Sars-Cov-2 Virion Protein and Structure. *Viruses* **2021**, *13*, 562.


https://doi.org/10.1021/acsami.2c15407
ACS Appl. Mater. Interfaces XXXX, XXX, XXX−XXX

(40) Karakuş, E.; Erdemir, E.; Demirbilek, N.; Liv, L. Colorimetric and Electrochemical Detection of SARS-CoV-2 Spike Antigen with a Gold Nanoparticle-Based Biosensor. *Anal. Chim. Acta* **2021**, *1182*, No. 338939.
(41) Guimarães, T. F.; Vital, I. C. F.; de Sousa, E. G. R.; Boniatti, J.; Bandini, T. B.; Carr, O.; Oliveira, O. N.; Shimizu, F. M.; da Fonseca, L. B.; Viçosa, A. L. Investigation of Chloroquine Resinate Feasibility and In Vitro Taste Masking Evaluation for Pediatric Formulations. *AAPS PharmSciTech* **2022**, *23*, No. 69.
(42) Bhattarai, K. R.; Kim, H. R.; Chae, H. J. Compliance with Saliva Collection Protocol in Healthy Volunteers: Strategies for Managing Risk and Errors. *Int. J. Med. Sci.* **2018**, *15*, 823−831.
(43) Peters, R. J. B.; van Bemmel, G.; Milani, N. B. L.; den Hertog, G. C. T.; Undas, A. K.; van der Lee, M.; Bouwmeester, H. Detection of Nanoparticles in Dutch Surface Waters. *Sci. Total Environ.* **2018**, *621*, 210−218.
(44) Zhang, L.; Mazouzi, Y.; Salmain, M.; Liedberg, B.; Boujday, S. Antibody-Gold Nanoparticle Bioconjugates for Biosensors: Synthesis, Characterization and Selected Applications. *Biosens. Bioelectron.* **2020**, *165*, No. 112370.
(45) Liao, H.; Hafner, J. H. Gold Nanorod Bioconjugates. *Chem. Mater.* **2005**, *17*, 4636−4641.
(46) Harron, D. W. G. Technical Requirements for Registration of Pharmaceuticals for Human Use: The ICH Process. In *The Textbook of Pharmaceutical Medicine*; Blackwell Publishing Ltd: Oxford, U.K., 2013; Vol. *1994*, pp 447−460. DOI: 10.1002/9781118532331.ch23.
(47) Johnson, P. B.; Christy, R. W. Optical Constants of the Noble Metals. *Phys. Rev. B* **1972**, *6*, 4370−4379.
(48) Baidya, S.; Hassan, A. M. A Computational Study of COVID-19 Detection Using Colorimetric Plasmonic Sensors. In *2021 IEEE International Symposium on Antennas and Propagation and USNC-URSI Radio Science Meeting (APS/URSI)*; IEEE, 2021; pp 1731−1732. DOI: 10.1109/APS/URSI47566.2021.9704523.
(49) Minopoli, A.; Scardapane, E.; Acunzo, A.; Campanile, R.; Della Ventura, B.; Velotta, R. Analysis of the Optical Response of a SARS-CoV-2-Directed Colorimetric Immunosensor. *AIP Adv.* **2021**, *11*, No. 065319.
(50) Ansar, S. M.; Chakraborty, S.; Kitchens, C. L. PH-Responsive Mercaptoundecanoic Acid Functionalized Gold Nanoparticles and Applications in Catalysis. *Nanomaterials* **2018**, *8*, 339.
(51) Raman, A.; Jaime, C.; Puntes, V. F. Domain Formation and Conformational Changes in Gold Nanoparticle Conjugates Studied Using DPD Simulations. *Langmuir* **2017**, *33*, 14502−14512.
(52) Fujiwara, K.; Watarai, H.; Itoh, H.; Nakahama, E.; Ogawa, N. Measurement of Antibody Binding to Protein Immobilized on Gold Nanoparticles by Localized Surface Plasmon Spectroscopy. *Anal. Bioanal. Chem.* **2006**, *386*, 639−644.
(53) Guvenc, B.; Yesilay, G.; Yavuz, Y.; Yilmaz, B.; Culha, M. Electrophysiological Effects of Polyethylene Glycol Modified Gold Nanoparticles on Mouse Hippocampal Neurons. *Heliyon* **2020**, *6*, No. e05824.
(54) Bravin, C.; Amendola, V. Plasmonic Absorption in Antigen-Induced Aggregated Gold Nanoparticles: Toward a Figure of Merit for Optical Nanosensors. *ACS Appl. Nano Mater.* **2022**, *5*, 578−586.
(55) Tsai, T. C.; Liu, C. W.; Wu, Y. C.; Ondevilla, N. A. P.; Osawa, M.; Chang, H. C. In Situ Study of EDC/NHS Immobilization on Gold Surface Based on Attenuated Total Reflection Surface-Enhanced Infrared Absorption Spectroscopy (ATR-SEIRAS). *Colloids Surf., B* **2019**, *175*, 300−305.
(56) Lee, J.; Zhou, H.; Lee, J. Small Molecule Induced Self-Assembly of Au Nanoparticles. *J. Mater. Chem.* **2011**, *21*, 16935.
(57) Busch, R. T.; Karim, F.; Weis, J.; Sun, Y.; Zhao, C.; Vasquez, E. S. Optimization and Structural Stability of Gold Nanoparticle-Antibody Bioconjugates. *ACS Omega* **2019**, *4*, 15269−15279.
(58) Ngunjiri, J. N.; Stark, D. J.; Tian, T.; Briggman, K. A.; Garno, J. C. Immobilization of Proteins on Carboxylic Acid Functionalized Nanopatterns. *Anal. Bioanal. Chem.* **2013**, *405*, 1985−1993.
(59) Sam, S.; Touahir, L.; Salvador Andresa, J.; Allongue, P.; Chazalviel, J. N.; Gouget-Laemmel, A. C.; De Villeneuve, C. H.; Moraillon, A.; Ozanam, F.; Gabouze, N.; Djebbar, S. Semiquantitative Study of the EDC/NHS Activation of Acid Terminal Groups at Modified Porous Silicon Surfaces. *Langmuir* **2010**, *26*, 809−814.
(60) Endo, T.; Kerman, K.; Nagatani, N.; Hiepa, H. M.; Kim, D. K.; Yonezawa, Y.; Nakano, K.; Tamiya, E. Multiple Label-Free Detection of Antigen-Antibody Reaction Using Localized Surface Plasmon Resonance-Based Core-Shell Structured Nanoparticle Layer Nano-chip. *Anal. Chem.* **2006**, *78*, 6465−6475.
(61) Meng, L.; Yin, J. H.; Yuan, Y.; Xu, N. 11-Mercaptoundecanoic Acid Capped Gold Nanoclusters as a Fluorescent Probe for Specific Detection of Folic Acid: Via a Ratiometric Fluorescence Strategy. *RSC Adv.* **2018**, *8*, 9327−9333.
(62) Garcia-Hernandez, C.; Freese, A. K.; Rodriguez-Mendez, M. L.; Wanekaya, A. K. In Situ Synthesis, Stabilization and Activity of Protein-Modified Gold Nanoparticles for Biological Applications. *Biomater. Sci.* **2019**, *7*, 2511−2519.
(63) Manson, J.; Kumar, D.; Meenan, B. J.; Dixon, D. Polyethylene Glycol Functionalized Gold Nanoparticles: The Influence of Capping Density on Stability in Various Media. *Gold Bull.* **2011**, *44*, 99−105.
(64) Moitra, P.; Alafeef, M.; Dighe, K.; Frieman, M. B.; Pan, D. Selective Naked-Eye Detection of SARS-CoV-2 Mediated by N Gene Targeted Antisense Oligonucleotide Capped Plasmonic Nano-particles. *ACS Nano* **2020**, *14*, 7617−7627.
(65) da Silva, P. B.; da Silva, J. R.; Rodrigues, M. C.; Vieira, J. A.; de Andrade, I. A.; Nagata, T.; Santos, A. S.; da Silva, S. W.; da Rocha, M. C. O.; Báo, S. N.; Moraes-Vieira, P. M.; Proença-Modena, J.; Angelim, M. K. C.; de Souza, G. F.; Muraro, S. P.; de Barros, A. L. B.; de Souza Martins, G. A.; Ribeiro-Dias, F.; Machado, G.; Fessel, M. R.; Chudzinski-Tavassi, A. M.; Ronconi, C. M.; Gonçalves, D.; Curi, R.; Oliveira, O. N.; Azevedo, R. B. Detection of SARS-CoV-2 Virus via Dynamic Light Scattering Using Antibody-Gold Nanoparticle Bioconjugates against Viral Spike Protein. *Talanta* **2022**, *243*, No. 123355.
(66) Brandl, D. W.; Mirin, N. A.; Nordlander, P. Plasmon Modes of Nanosphere Trimers and Quadrumers. *J. Phys. Chem. B* **2006**, *110*, 12302−12310.
(67) Raikar, U. S.; Tangod, V. B.; Mastiholi, B. M.; Fulari, V. J. Fluorescence Quenching Using Plasmonic Gold Nanoparticles. *Opt. Commun.* **2011**, *284*, 4761−4765.
(68) Zhang, Y.; Fei, W.-W.; Jia, N.-Q. A Facile Method for the Detection of DNA by Using Gold Nanoparticle Probes Coupled with Dynamic Light Scattering. *Nanoscale Res. Lett.* **2012**, *7*, No. 564.
(69) Paulovich, F. V.; Moraes, M. L.; Maki, R. M.; Ferreira, M.; Oliveira, O. N., Jr.; de Oliveira, M. C. F. Information Visualization Techniques for Sensing and Biosensing. *Analyst* **2011**, *136*, 1344.
(70) Neto, M. P.; Paulovich, F. V. Explainable Matrix - Visualization for Global and Local Interpretability of Random Forest Classification Ensembles. *IEEE Trans. Visual Comput. Graphics* **2021**, *27*, 1427−1437.
(71) Ihsanullah, I.; Bilal, M.; Naushad, M. Coronavirus 2 (SARS-CoV-2) in Water Environments: Current Status, Challenges and Research Opportunities. *J. Water Process Eng.* **2021**, *39*, No. 101735.
(72) Woolf, M. S.; Dignan, L. M.; Scott, A. T.; Landers, J. P. Digital Postprocessing and Image Segmentation for Objective Analysis of Colorimetric Reactions. *Nat. Protoc.* **2021**, *16*, 218−238.
(73) Brinati, D.; Campagner, A.; Ferrari, D.; Locatelli, M.; Banfi, G.; Cabitza, F. Detection of COVID-19 Infection from Routine Blood Exams with Machine Learning: A Feasibility Study. *J. Med. Syst.* **2020**, *44*, No. 135.


https://doi.org/10.1021/acsami.2c15407
*ACS Appl. Mater. Interfaces* XXXX, XXX, XXX−XXX